

Structure and Spectroelectrochemical Response of Arene–Ruthenium and Arene–Osmium Complexes with Potentially Hemilabile Noninnocent Ligands

Martina Bubrin,[†] David Schweinfurth,^{†,‡} Fabian Ehret,[†] Stanislav Zálíš,[§] Hana Kvapilová,[§] Jan Fiedler,[§] Qiang Zeng,^{||} František Hartl,^{*,||} and Wolfgang Kaim^{*,†}

[†]Institut für Anorganische Chemie, Universität Stuttgart, Pfaffenwaldring 55, D-70550 Stuttgart, Germany

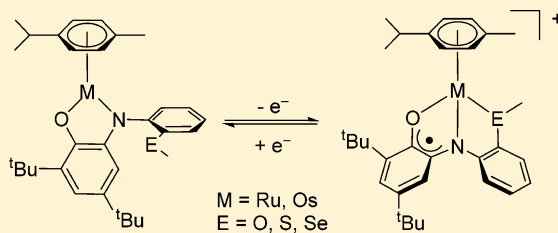
[‡]Institut für Chemie und Biochemie, Freie Universität Berlin, Fabeckstraße 34-36, D- 14195 Berlin, Germany

[§]J. Heyrovský Institute of Physical Chemistry, v.v.i., Academy of Sciences of the Czech Republic, Dolejškova 3, CZ-18223 Prague, Czech Republic

^{||}Department of Chemistry, University of Reading, Whiteknights, Reading RG6 6AD, United Kingdom

S Supporting Information

ABSTRACT: Nine of the compounds $[M(L^{2-})(p\text{-cymene})]$ ($M = \text{Ru}, \text{Os}$, $L^{2-} = 4,6\text{-di-}t\text{-butyl-}N\text{-aryl-}o\text{-amidophenolate}$) were prepared and structurally characterized (Ru complexes) as coordinatively unsaturated, formally 16 valence electron species. On L^{2-} -ligand based oxidation to EPR-active iminosemiquinone radical complexes, the compounds seek to bind a donor atom (if available) from the N -aryl substituent, as structurally certified for thioether and selenoether functions, or from the donor solvent. Simulated cyclic voltammograms and spectroelectrochemistry at ambient and low temperatures in combination with DFT results confirm a square scheme behavior (ECEC mechanism) involving the L^n ligand as the main electron transfer site and the metal with fractional (δ) oxidation as the center for redox-activated coordination. Attempts to crystallize $[\text{Ru}(\text{Cym})(\text{Q}_{\text{SMe}})](\text{PF}_6)$ produced single crystals of $[\text{Ru}^{\text{III}}(\text{Q}_{\text{SMe}}^{\bullet-})_2](\text{PF}_6)$ after apparent dissociation of the arene ligand.

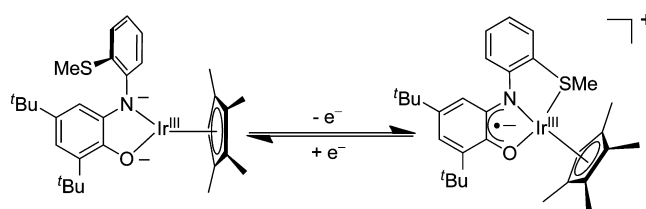


INTRODUCTION

In 2008 Ringenberg, Rauchfuss, et al. reported the organometallic system $[\text{Ir}(\text{C}_5\text{Me}_5)\text{Q}]^{+/0}$ ($(\text{Q}')^{2-} = 4,6\text{-di-}t\text{-butyl-}2\text{-}(2\text{-trifluoromethyl)amidophenolate}$), which was shown¹ to catalyze the “hydrogenase-type” conversion of H_2 to H^+ via electron transfer based on the noninnocent² amidophenolate/imino benzosemiquinone ligand redox system.³ While an extension of this work focusing on the role of external base was provided later,⁴ including a brief reference to a related (inactive) areneruthenium species, we have studied the underlying reactivity in the form of a reversible single-electron oxidation-induced addition in an intramolecular arrangement (Chart 1) for $[\text{Ir}(\text{C}_5\text{Me}_5)\text{Q}_y]^{+/0}$,⁵ making use of the hemilabile character of this previously introduced⁷ ligand $\text{Q}_y^{2-} = 4,6\text{-di-}t\text{-butyl-}2\text{-}(2\text{-methylthio)amidophenolate}$.

Spectroscopic (EPR) and DFT investigations revealed an activation involving minor (ca. 8%) but non-negligible spin density transfer from the ligand to the metal as a crucial feature.⁵ Modifications including rhodium analogues and the effect of thioether/ether (S/O donor) substituent exchange were studied,⁸ using the noninnocent⁷ amidophenolate/imino semiquinone/imino benzquinone redox systems³ as represented by o -imino semiquinonate ligand intermediates $\text{Q}_{\text{SMe}}^{\bullet-}$ and $\text{Q}_{\text{OMe}}^{\bullet-}$ (see Chart 2).

Chart 1. Reversible Intramolecular 1e Oxidation-Induced Addition⁵

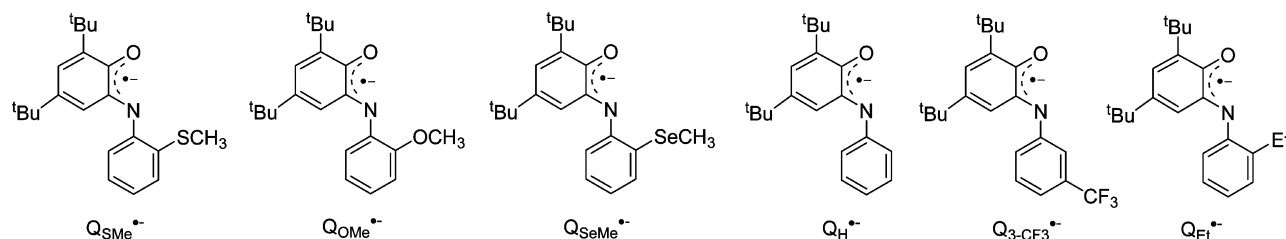


In this report we describe the synthesis, partial structural characterization, cyclic voltammetry, and spectroelectrochemistry at ambient and low temperatures⁹ of neutral and cationic complexes of $(\eta^6\text{-Cym})\text{M}$ ($\text{Cym} = p\text{-cymene}$, $\text{M} = \text{Ru}, \text{Os}$) with the noninnocent ligands in Chart 2 (iminosemiquinone forms shown).

Arene–ruthenium and –osmium complexes have been widely used in catalysis¹⁰ and in the development of metallodrugs.¹¹

Special Issue: Organometallic Electrochemistry

Received: March 17, 2014

Chart 2. *o*-Iminosemiquinonate Ligands

RESULTS AND DISCUSSION

Synthesis and Characterization. The neutral compounds 1–9 (Chart 3) were obtained from the reaction of the

Chart 3. Compounds Investigated

$[\text{Ru}(\text{Cym})(\text{Q}_{\text{SMe}})]$	1
$[\text{Ru}(\text{Cym})(\text{Q}_{\text{SMe}})](\text{BAR}^{\text{F}})$	[1](BAR^F)
$[\text{Ru}(\text{Cym})(\text{Q}_{\text{OMe}})]$	2
$[\text{Ru}(\text{Cym})(\text{Q}_{\text{SeMe}})]$	3
$[\text{Ru}(\text{Cym})(\text{Q}_{\text{SeMe}})](\text{BAR}^{\text{F}})$	[3](BAR^F)
$[\text{Ru}(\text{Cym})(\text{Q}_{\text{H}})]$	4
$[\text{Ru}(\text{Cym})(\text{Q}_{3\text{-CF}_3})]$	5
$[\text{Ru}(\text{Cym})(\text{Q}_{\text{Et}})]$	6
$[\text{Os}(\text{Cym})(\text{Q}_{\text{SMe}})]$	7
$[\text{Os}(\text{Cym})(\text{Q}_{\text{OMe}})]$	8
$[\text{Os}(\text{Cym})(\text{Q}_{\text{SeMe}})]$	9
$[\text{Ru}(\text{Q}_{\text{SMe}})_2](\text{PF}_6)$	[10](PF₆)

corresponding *o*-aminophenol precursors and $[\text{M}(\text{Cym})\text{Cl}_2]_2$ under basic conditions. The ruthenium compounds 1–6 are more stable than the osmium complexes 7–9, which is attributed to more facile dissociation of the neutral aromatic cymene ligand. All compounds proved to be air sensitive and slowly reacted (within days) with dichloromethane; crystallization was thus performed from other solvents (see the Experimental Section). Oxidation using $\text{Fc}(\text{BAR}^{\text{F}})$ ($\text{BAR}^{\text{F}-} = \text{tetrakis}(3,5\text{-bis}(\text{trifluoromethyl})\text{phenyl})\text{borate}$)¹² was successful for the ruthenium compounds 1 and 3 to yield structurally characterized salts with the noncoordinating $\text{BAR}^{\text{F}-}$ anion. Similar attempts to oxidize other complexes such as 2 resulted in noncrystalline material, probably due to the lack of strong intramolecular addition (2, 4–6) or because of the generally higher lability in the case of the osmium analogues 7–9. During the attempted crystallization of $[\text{Ru}(\text{Cym})(\text{Q}_{\text{SMe}})](\text{PF}_6)$ the formation of **[10](PF₆)** was observed, as confirmed by a single-crystal X-ray analysis. This reaction involves dissociation of neutral arene and produces a paramagnetic cation which had been characterized

spectroelectrochemically (EPR, UV–vis–NIR) earlier.¹³ A structural comparison will be made below between $[\text{Ru}(\text{Q}_{\text{SMe}})_2]^+$ (**10**) and the neutral precursor $[\text{Ru}(\text{Q}_{\text{SMe}})_2]$, aimed at assignment of the oxidation states of the metal center and of the noninnocent ligands.

Structure. In the crystallographically characterized (Table 1 and Table S1 (Supporting Information), Figures 1–5 and Figures S1–S4 (Supporting Information)) neutral compounds 1–6 the metal exhibits a formal 16-valence-electron count. Such coordinative unsaturation was observed before for metal catecholate compounds of, e.g., Cr, W, Mn, Re, Rh, and Ir;^{5,8,14–16} it is attributable to the strong σ and π donation from the catecholate dianion. The bond parameters of the neutral compounds are very similar (Table 1) and are well reproduced for 1–5 by DFT calculations (Tables S2 and S3 (Supporting Information)). No unusual intermolecular interactions have been observed (Figure S4). The neutral compounds 1 and 3 are isostructural (S/Se exchange). The *p*-cymene ligands adopt different orientations in the crystals, as illustrated in Figure S5. The *N*-aryl substituents are substantially twisted relative to the amidophenolate chelate ring (cf. the angle ω in Table 1), illustrating the lack of conjugation as well as the nonbonded interactions ($\text{Ru} \cdots \text{E} \geq 3.95 \text{ \AA}$) of the chalcogen heteroatoms O (2), S (1), and Se (3).

The redox pairs $1/1^+$ and $3/3^+$ illustrate the structural effect of oxidation: the Ru–N and, to a lesser extent, the Ru–O distances increase. The *o*-monoiminoquinones have become popular^{17–19} due to their strong metal binding even in the neutral form while offering easy access to all three oxidation states in the conventional redox potential region. In contrast to the Ru–N and Ru–O bond lengths, the C–O and C–N distances decrease by about 0.02 Å, indicating electron loss from the amidophenolate ligand. In fact, the EPR data for all cations (see below) show an *o*-iminosemiquinone spin distribution. The C–C distances in the aromatic rings correspond to averaged values for the amidophenolate compounds but reveal the onset of bond alternation in the semiquinone complexes.

Most significantly, the oxidized complexes complement their coordination by binding the S (1^+) or Se (3^+) donor atoms at a normal bond length of about 2.4 Å. A twist is necessary to effect this, the dihedral angles between the *N*-aryl substituents relative to the aminophenolate chelate ring being forced to decrease to $<60^\circ$.

As noted earlier,^{5,8} the oxidation of the complex may affect predominantly the noninnocent ligand (see below) but the fractional amount δ of the charge change at the metal results in additional coordination of the hemilabile ligand. The additional binding of the thio- and selenoether donors in systems $1/1^+$ and $3/3^+$, respectively, appears reasonable but raises further questions: How does an *O*-ether function respond, are coordination situations comparable for solids and dissolved

Table 1. Selected Atom–Atom Distances (Å) and Dihedral Angles (deg)

	1	1 ⁺	2	3	3 ⁺	4	5	6
Ru–N	1.963(5)	2.043(2) 2.048(2)	1.952(2)	1.967(5)	2.045(2)	1.949(2) 1.952(2)	1.951(1)	1.967(4) 1.963(4)
Ru–O	2.003(3)	2.049(2) 2.048(2)	2.022(2)	2.005(5)	2.048(1)	2.005(2) 2.006(2)	2.000(1)	2.017(3) 2.022(3)
C–O	1.327(6)	1.309(3) 1.309(3)	1.341(3)	1.332(8)	1.312(3)	1.339(3) 1.338(3)	1.336(2)	1.330(6) 1.337(5)
C–N	1.395(6)	1.372(3) 1.373(3)	1.396(3)	1.411(9)	1.369(3)	1.398(3) 1.393(3)	1.393(2)	1.383(6) 1.386(6)
C1–C2	1.401(8)	1.426(4) 1.425(4)	1.402(4)	1.415(9)	1.424(4)	1.405(3) 1.412(3)	1.410(2)	1.398(6) 1.396(6)
C2–C3	1.401(8)	1.406(4) 1.405(4)	1.398(4)	1.394(9)	1.409(4)	1.402(3) 1.407(3)	1.403(2)	1.413/(7) 1.409(6)
C3–C4	1.388(7)	1.368(4) 1.375(4)	1.377(4)	1.379(9)	1.371(4)	1.387(3) 1.381(3)	1.388(2)	1.384(6) 1.388(6)
C4–C5	1.412(7)	1.421(4) 1.420(4)	1.405(4)	1.410(9)	1.431(4)	1.415(3) 1.412(3)	1.416(2)	1.409(6) 1.415(7)
C5–C6	1.388(8)	1.378(4) 1.383(4)	1.387(4)	1.385(9)	1.375(4)	1.396(3) 1.395(3)	1.389(2)	1.388(7) 1.392(6)
C1–C6	1.421(7)	1.438(4) 1.432(4)	1.419(3)	1.424(9)	1.434(4)	1.415(3) 1.412(3)	1.424(2)	1.425(6) 1.420(6)
Ru–E ^a	3.949(3)	2.3820(8) 2.3806(8)	4.094(2)	4.002(2)	2.508(0)			
ω^b	81.27	53.62 59.24	72.45	80.61	58.43	85.65 88.09	63.56	81.59 79.95

^aE = S, O. ^bDihedral angle between N-aryl substituent and chelate ring.

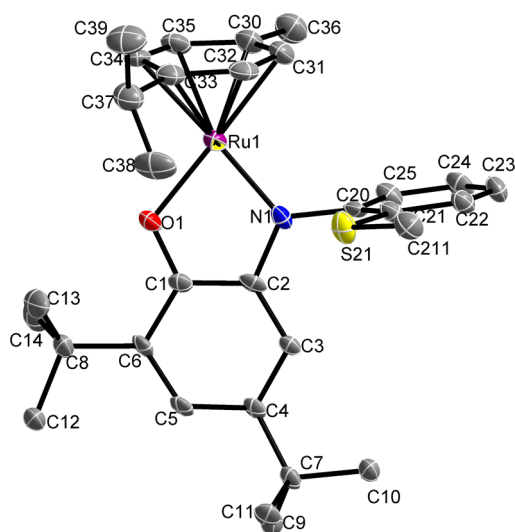


Figure 1. Molecular structure of **1** in the crystal. Thermal ellipsoids are given at the 50% probability level.

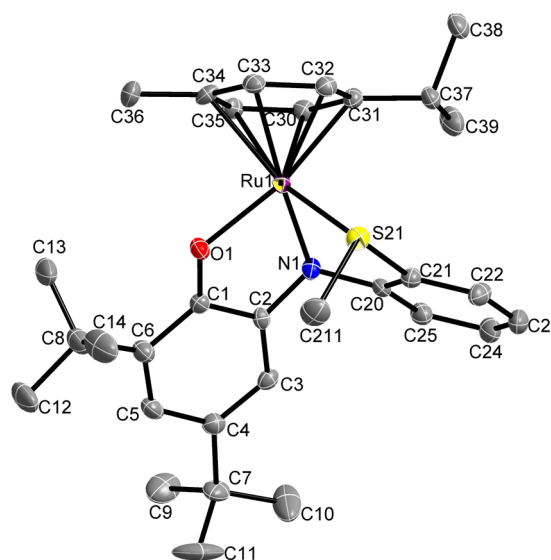


Figure 2. Molecular structure of the cation in the crystal of **[1](BARF)**. Thermal ellipsoids are given at the 50% probability level.

complexes, and which options are there in the absence of suitable complementary donor atoms within the noninnocent ligand?

The DFT calculations on **1/1⁺** and **7/7⁺** confirm the lower energy of the *S*-noncoordinated form for the neutral species and the *S*-coordinated arrangement for the cations; the alternatives, *S*-coordinated neutral and *S*-dissociated cation (Scheme 1), have been calculated at significantly higher energies. In vacuo DFT calculated selected bond lengths and angles of complexes are given in Tables S2–S4 (Supporting Information). The calculated bonding parameters agree with the experimental structural data for the ruthenium compounds (Table 1). Both configurations, i.e., the *N,O*-bonded (form **A**, Chart 4) and *N,O,S*-coordinated

alternatives (form **B**), were examined for the complexes **1** and **7**. In the case of the neutral species the calculations indicate that form **A** is more stable; free energy differences, ΔG , of 0.407 and 0.506 eV have been obtained for the neutral Ru (**1**) and Os (**7**) complexes, respectively. Form **B** is more stable for the monooxidized species, where ΔG values of 0.339 and 0.324 eV have been obtained for Ru (**1⁺**) and Os (**7⁺**) complexes, respectively.

Attempts to crystallize $[\text{Ru}(\text{Cym})(\text{Q}_{\text{SMc}})](\text{PF}_6)$ from dichloromethane led to the formation of single crystals of the compound **[10](PF₆)** (Table S5 (Supporting Information)). Apparently, dissociation of the neutral arene ligand has taken

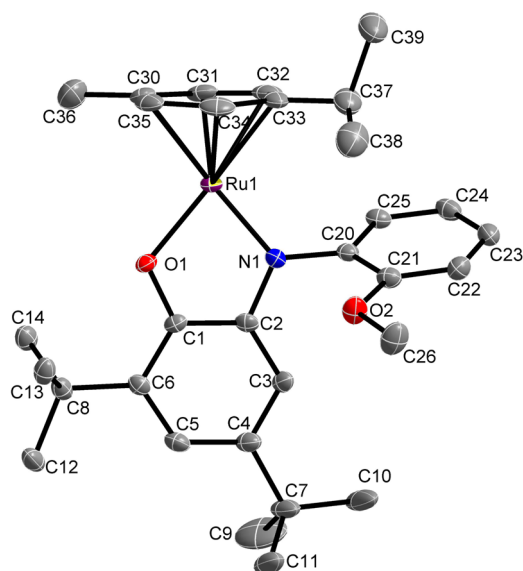


Figure 3. Molecular structure of **2** in the crystal. Thermal ellipsoids are given at the 50% probability level.

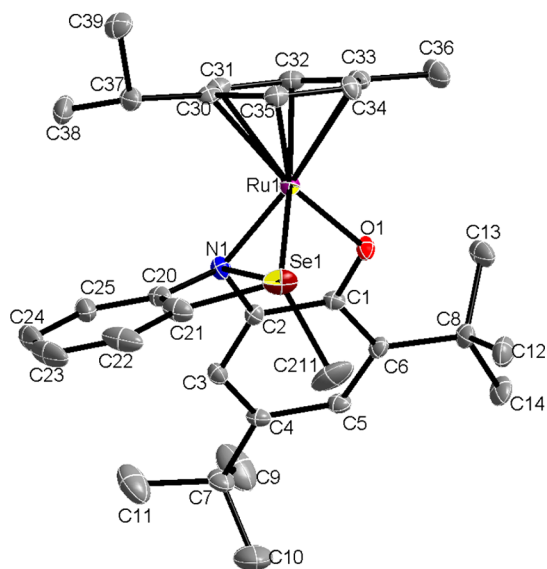


Figure 4. Molecular structure of the cation in the crystal of $[3](\text{BARF})$. Thermal ellipsoids are given at the 50% probability level.

place (Scheme 1). While the neutral precursor **10**, identified structurally as $[\text{Ru}^{\text{IV}}(\text{Q}_{\text{SMe}}^{2-})_2]$, had been characterized spectroelectrochemically (EPR, UV–vis–NIR) earlier,¹³ the presently feasible structural comparison of **10** and **10**⁺ (Table S6 and Figure S6 (Supporting Information)) reveals that the oxidation to **10**⁺ produces a situation best described as $[\text{Ru}^{\text{III}}(\text{Q}_{\text{SMe}}^{\bullet-})_2]^+$. Accordingly, a redox-induced electron transfer (RIET)²⁰ has effected metal reduction as a consequence of double ligand oxidation (Scheme 2), evident especially by shortened CO and CN bonds. Another structural difference between $[\mathbf{10}](\text{PF}_6)$ and the neutral precursor **10** involves the CC bonds in the six-membered ring, which change from average values around 1.40 Å to more alternating bond lengths, as may be expected for semiquinones (Table S6).

Cyclic Voltammetry. All neutral compounds **1–9** undergo two-step oxidation processes in the accessible potential range in $\text{CH}_2\text{Cl}_2/0.1 \text{ M Bu}_4\text{NPF}_6$ solution. However, the redox

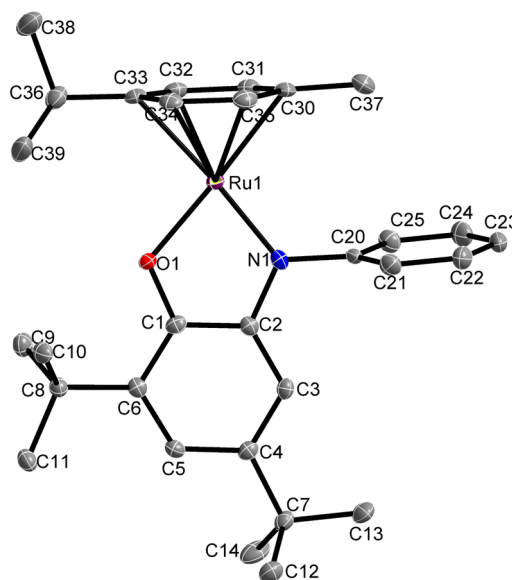


Figure 5. Molecular structure of **4** in the crystal (one of the two independent molecules in the unit cell). Thermal ellipsoids are given at the 50% probability level.

mechanism and the cyclic voltammetric response depend on the coordination capabilities of the iminosemiquinonate ligands.

Compounds **4–6** without a hemilabile ligand, i.e., without intramolecularly accessible donors, exhibit in CH_2Cl_2 only one indiscernible wave (see Figure 6, top, for system **4**ⁿ), comprising two potentially close 1e steps (cf. detection of cation radicals by EPR). Simple charge transfers without a coupled chemical reaction can be expected in the absence of the auxiliary coordinating functionality and in noncoordinating CH_2Cl_2 . In a coordinating solvent the situation is changed, as illustrated in Figure 6. The use of coordinating CH_3CN results in a larger separation between the anodic oxidation waves and the shifted reverse cathodic waves for the first redox step, **4**/**4**⁺, obviously coupled with CH_3CN coordination. The second redox process, **4**⁺/**4**²⁺, displays normal Nernstian behavior, indicating unchanged coordination of the 18-valence-electron species (Figure 6, bottom).

The compounds **1–3** and **7–9** with potential for intramolecular chalcogen coordination exhibit in the first step a response characteristic of a square redox scheme (Figures 7–9 and Figures S7–S10 (Supporting Information)) with a strongly shifted reverse cathodic wave (Scheme 3, Table 2), as has been presented for the related redox system $[\text{Ir}(\text{C}_5\text{Me}_5)\text{Q}_2]^+/0$ (**11**/**11**⁺). The follow-up reaction with an electrochemically manifested structural change accompanying the first electron transfer process (neutral/cation) contrasts markedly with the Nernstian behavior of the second oxidation step (cation/dication), suggesting the absence of significant structural changes in this case.

Apparently, the initial electron withdrawal of an electron from neutral, coordinatively unsaturated 16-VE species at virtually substituent-independent potentials (Table 2) leads to an unstable cationic complex which tends to achieve coordinative saturation either by an intramolecular process (**1–3**, **7–9**) or through the binding of coordinating solvent molecules (**4–6**). On second oxidation, the “piano-stool” coordination arrangement remains unchanged, as illustrated by the apparently reversible waves.

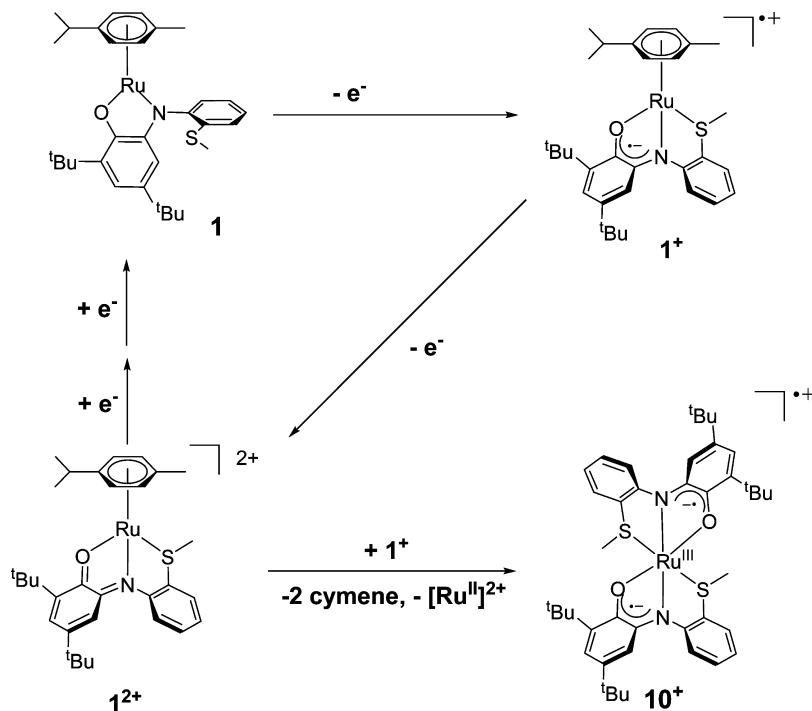
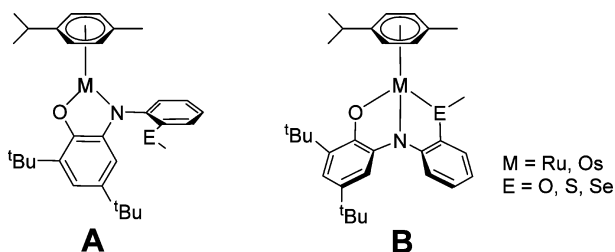
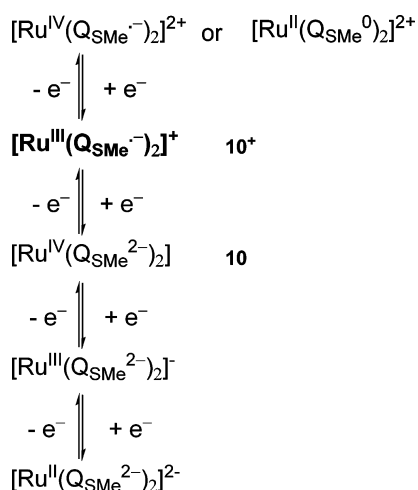
Scheme 1. Anodic Conversion of Compound 1 to Radical Cation 10⁺

Chart 4. Bonding Alternatives for Hemilabile Noninnocent Ligands

Scheme 2. Redox Series of $[\text{Ru}(\text{Q}_{\text{SMe}})_2]^n$ 

After the first cycling the cyclic voltammograms of the isolated oxidized compounds [**1**](BAR^F) and [**3**](BAR^F) showed the same response (Figure 8) as those of the neutral precursors.

The forward anodic and reverse cathodic voltammetric responses of complexes **1–3**, **7**, and **9** were simulated (Figures

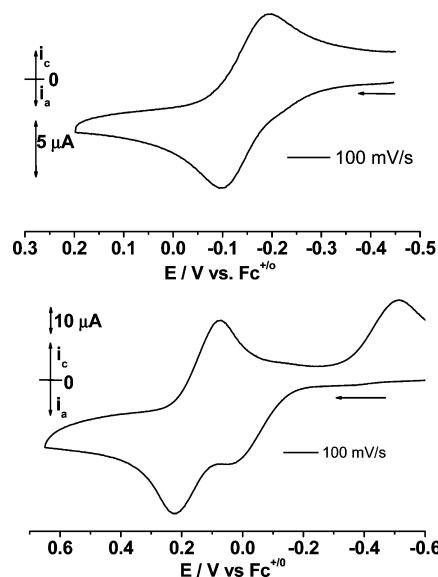


Figure 6. Cyclic voltammograms of **4** in CH_2Cl_2 (top) and CH_3CN (bottom), with each complex in 0.1 M $\text{Bu}_4\text{NPF}_6/\text{CH}_2\text{Cl}_2$ at 298 K.

7 and **8**). The derived parameters in Table 3 reveal reasonable differences: the small values of equilibrium constants K_1 (for the cations) and K_2 (for the neutral species) confirm the weak bonding for the ether complex. Even at lower temperatures (253 K) the O-donor system **2^x** still exhibits K_1 constants considerably smaller than those of the other systems investigated. However, a much increased constant K_2 was determined for **2^x** at low temperature, reflecting the absence of O-coordination.

The rate constants k_1 obtained from simulations also reflect more rapid association of the E-donor functionality to the metal after oxidation for **2^x** in comparison to the thio- and selenoether analogues **1^x** and **3^x**; the osmium complexes **7^x** and **9^x** are

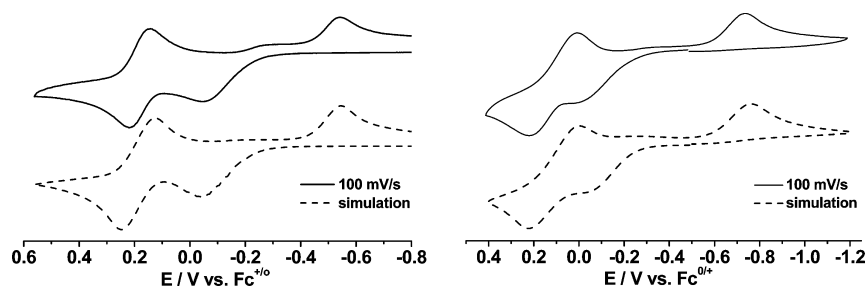


Figure 7. Cyclic voltammograms of **1** (left) and **3** (right) in 0.1 M Bu₄NPF₆/CH₂Cl₂ at 298 K with simulation (for parameters see Scheme 3 and text).

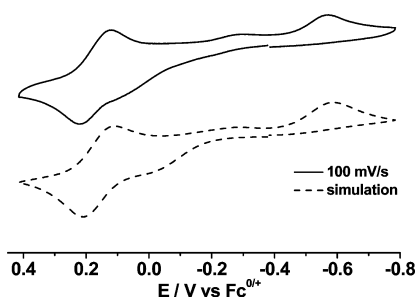


Figure 8. Cyclic voltammogram of **7** in 0.1 M Bu₄NPF₆/CH₂Cl₂ at 298 K with simulation (for parameters see Scheme 3 and text).

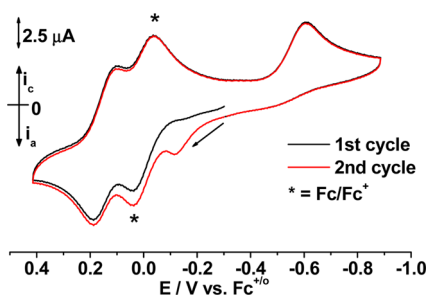


Figure 9. Cyclic voltammograms of **[1](BARF)** at 100 mV/s at 298 K in 0.1 M Bu₄NPF₆/CH₂Cl₂.

distinguished by slower reactions.³ The k_2 values for dissociation of the E-donor functions are invariably much larger than k_1 .

EPR Spectroscopy. The one-electron-oxidized intermediates **1**⁺–**9**⁺ are paramagnetic and thus susceptible to investigation by EPR. The recorded experimental and corresponding simulated spectra are shown in Figure 10; the EPR data are given in Table 4.

All spectra indicate predominant oxidation of the amidophenolate to the iminosemiquinonato ligand, exhibiting

- high EPR resolution at room temperature in solution
- isotropic g factors close to the free electron value of 2.0023
- unresolved small g anisotropy $g_1 - g_3$ in the glassy frozen state
- ¹⁴N and ¹H hyperfine coupling constants typical for *o*-iminosemiquinones
- metal isotope hyperfine splitting at only a fraction (<0.012) of the corresponding isotropic hyperfine coupling constant ($A_{\text{iso}} = -629.4$ G for ⁹⁹Ru (12.7% natural abundance), -705.2 G for ¹⁰¹Ru (17.0% natural abundance), 4710 G for ¹⁸⁹Os (16.1% natural abundance)).²¹

While the values do not vary excessively, there are revealing differences which pertain also to those species which could not be

crystallized: the osmium systems are distinguished by a distinctly lower g factor due to the very high spin–orbit coupling constant of the 5d transition metal^{21,22} and by large metal hyperfine splitting due to the high A_{iso} value of 4710 G.²¹ The radical complex **8**⁺ could not be investigated due to its lability. The deviation to smaller g values reflects the proximity of empty orbitals near the singly occupied MO (SOMO),^{23,24} and the relatively small a/A_{iso} ratios of <0.010 point to decreased covalent nature of the metal–ligand bonding. The $a(\text{H})$ constant from H5 at the amidophenolate ring reflects, like the ¹⁴N splitting, variable spin distribution as caused by different binding of O, S, or Se “arms” (intramolecularly) or by the solvent. Rather large differences between $a(^{99,101}\text{Ru})$ values are attributed to the weaker bonding of the ether (**2**⁺) or solvent ligands (**4**⁺–**6**⁺, smaller values <6 G) with respect to thio- or selenoether groups, which leads to higher metal splitting constants (>8.0 G).

Table S7 (Supporting Information) gives G09/PBE0/PCM calculated spin densities for all cationic species. The spin density distribution in both forms of the radical cation **1**⁺ is depicted in Figure 11. Ruthenium spin densities are calculated at 0.07 and 0.16 for forms **B** and **A**, respectively. The calculations on the complex **7**⁺ (form **B**) give a spin density of 0.095 on the Os atom. As for the reported iridium complex ion **11**⁺, the DFT calculations thus suggest relatively low spin densities on the metals (Ru or Os), in agreement with the observed EPR characteristics. Calculated spin densities show higher metal contribution for radical complexes **2**⁺–**5**⁺ and **7**⁺ lacking the thioether coordination. Larger metal and smaller ligand spin densities were calculated for the *S*-noncoordinated structure **A** of **1**⁺ (see Figure 11).

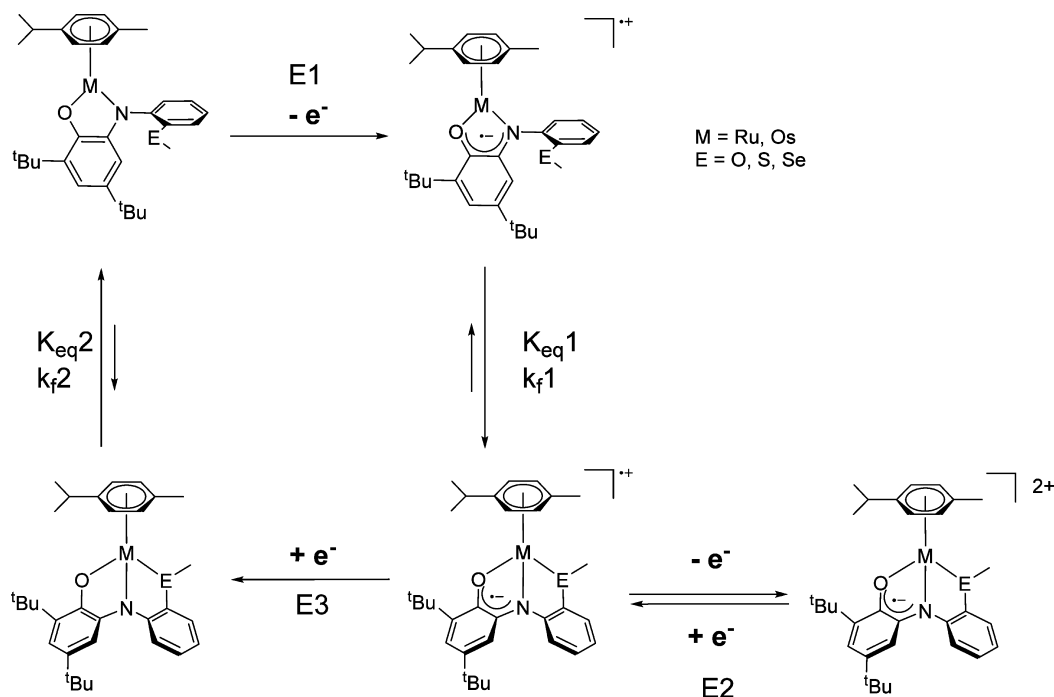
While the EPR results confirm that a small (“ δ ”) ligand-to-metal spin transfer can effect a significant change in the coordination behavior, the related ruthenium system [Ru(Cym)(Q)]^{0/+}, as described and characterized by Ringenberg et al.,^{4a} showed no catalytic activity toward dihydrogen conversion.

UV–Vis–NIR Spectroelectrochemistry. Both oxidation processes of the compounds **1**–**9** could be monitored by spectroelectrochemistry at 293 and 223 K using OTTL cells (see the Experimental Section). Figures 12 and 13 and Figures S11–S13 (Supporting Information) show representative responses, and Table 5 summarizes the observed absorptions.

Low-temperature spectroelectrochemistry was utilized to generate unstable dications from the osmium complexes. The cations **7**²⁺ and **8**²⁺ obtained by fast electrolysis at the second oxidation peak have then been rereduced in the reverse potential scan to monocations and subsequently to the neutral original complexes (Figure 13 and Figure S13 (Supporting Information)).

The neutral precursor molecules exhibit LMCT bands at about 500 nm ($M = \text{Ru}$) or 400 nm ($M = \text{Os}$). A representative TD DFT calculation of **1** yields an intense transition at 427 nm, the

Scheme 3. Redox Cycle As Derived from Cyclic Voltammetry

Table 2. Redox Potentials^a from Cyclic Voltammetry in CH₂Cl₂/0.1 M Bu₄NPF₆ at 100 mV/s Scan Rate

redox system	first oxidation		second oxidation $E_{1/2}$
	E_{pa}	E_{pc}	
1 ⁿ	-0.07	-0.54	0.18
2 ⁿ	-0.05	-0.40	0.10
3 ⁿ	-0.04	-0.74	0.11
4 ⁿ		-0.14 ^b	
5 ⁿ		-0.13 ^b	
6 ⁿ		-0.09 ^b	
7 ⁿ	-0.07	-0.20	0.19
8 ⁿ	0.12	-0.08	0.06
9 ⁿ	-0.01	-0.40	0.19

^aIn V vs Fc/Fc⁺. ^b $E_{1/2}$.

Table 3. Equilibrium Constants and Rates Obtained from Simulations of Cyclic Voltammograms^a

	$K_{eq}(1); k_f(1)/s^{-1}$	$K_{eq}(2); k_f(2)/s^{-1}$	het rate constant $k_s/cm s^{-1}$	diffusion coeff/cm ² s ⁻¹
1	$4.6 \times 10^4; 4.5$	$4.1 \times 10^4; 1.66 \times 10^8$	0.1	9×10^{-5}
3	$4.5 \times 10^5; 3.0$	$1.6 \times 10^5; 1.2 \times 10^{10}$	0.005	7×10^{-5}
2	58.2; 380	$2.016; 5.7 \times 10^{10}$	0.02	7×10^{-5}
2 (253 K)	$2.42 \times 10^2; 0.16$	$8.4 \times 10^5; 1.1 \times 10^9$	n.d.	n.d.
7	$1.7 \times 10^4; 0.48$	$1.2 \times 10^5; 5.8 \times 10^9$	0.005	5.4×10^{-5}
9	$4.2 \times 10^4; 0.95$	$2.8 \times 10^4; 3.9 \times 10^7$	0.02	7×10^{-5}

^aSee Scheme 3 and Figures 6 and 7; $R_{int} = 800 \Omega$. $T = 293$ K unless noted otherwise.

MLCT character of which is illustrated in Figure S14 (Supporting Information). On the first oxidation to the semiquinone state (see EPR Spectroscopy), the diminished

MLCT band is shifted and a broad absorption appears in the vis–NIR border region (700–1000 nm). This feature is assigned to a weak mixed intraligand/metal centered (IL/MC) transition (Figure S15 (Supporting Information)), calculated for 1⁺ at 784 nm.

CONCLUSIONS

The crystallographically characterized redox pairs 1/1⁺ and 3/3⁺ involving ruthenium show behavior similar to that of the related iridium-based system 11/11⁺ and that of the corresponding osmium analogues 7/7⁺ and 9/9⁺. Reversible intramolecular one-electron oxidative addition to effect a tridentate coordination of the respective hemilabile noninnocent ligands takes place with predominant, albeit not exclusive, spin concentration at the semiquinone part of the ligand. The small amount δ of charge transferred from the metal is apparently sufficient to cause binding of S (1, 11), Se (3), or external H₂ ligands.¹ The simulated cyclic voltammetric response and the spectroelectrochemical characterization allowed us to analyze the mechanism of Scheme 3 in quantitative detail. The situation in the oxidized O-ether compound 2⁺, in the complexes 4⁺–6⁺ with pendant donor-free bidentate ligands, and in the osmium analogues 7⁺–9⁺ was not accessible by structure determination in the solid. However, the (spectro)electrochemical results point to similar behavior of more weakly bonded OMe substituents (2⁺, 8⁺), coordinating solvent molecules (4⁺–6⁺), or analogously appended thio- and selenoether functions (7⁺, 9⁺). The corresponding equilibrium constants, which also reflect possible differences between dissolved molecules and those packed in the crystal, have been determined for representative cases through simulation of voltammograms. In the absence of additional donor functions from the ligand or the solvent, two one-electron reversible oxidations at close potentials are observed, merged into a single wave in the cyclic voltammetry experiment. In all cases, the EPR information about g factors and about metal and

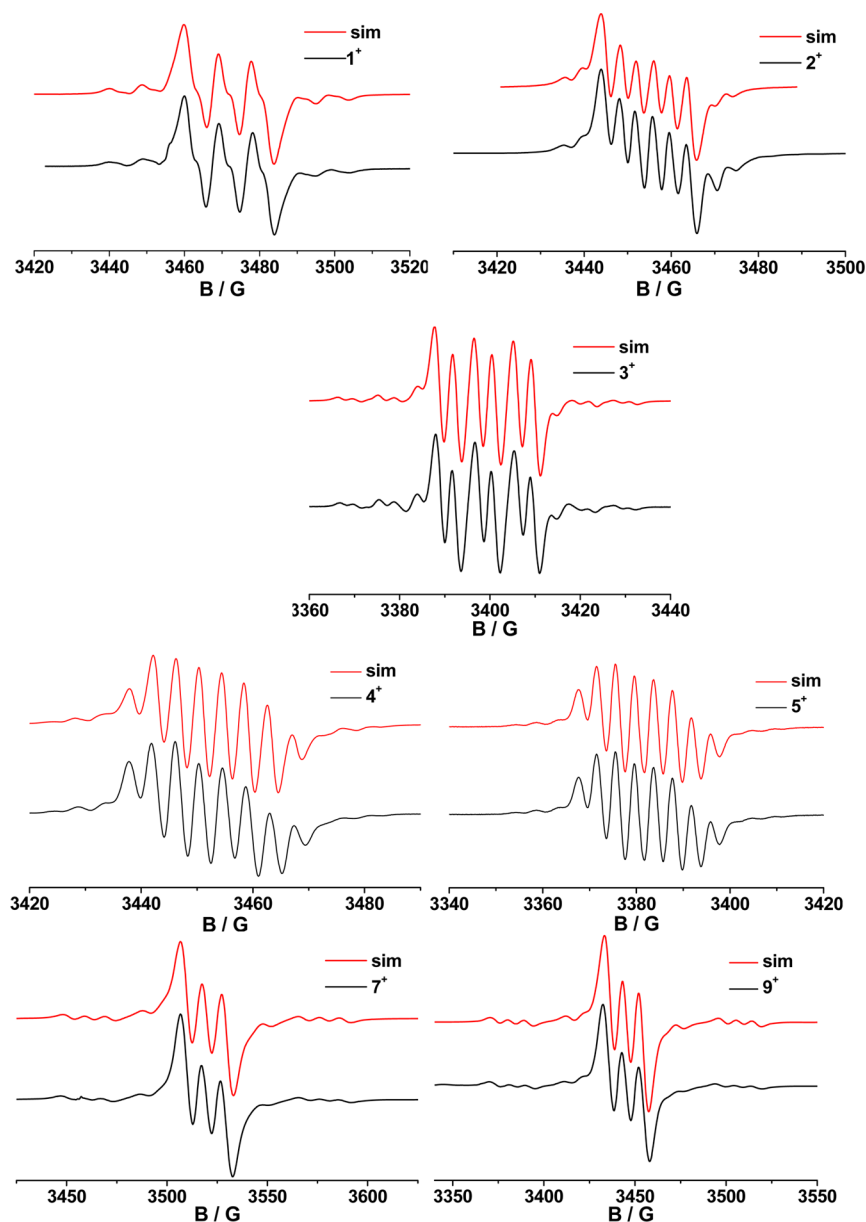


Figure 10. EPR spectra (with simulations) of 1^+ (top left), 2^+ (top right), 3^+ (center), 4^+ (center left), 5^+ (center right), 7^+ (bottom left), and 9^+ (bottom right) at 298 K in CH_2Cl_2 (from oxidation with FcPF_6 ; $1 \text{ G} = 10^{-4} \text{ mT}$).

Table 4. EPR Parameters of Radical Complex Cations^a

	1^+	2^+	3^+	4^+	6^+	5^+	7^+	9^+
g	1.992	2.002	1.989	2.000	1.999	2.000	1.965	1.962
$a(^{14}\text{N})$	8.7	7.6	8.7	8.0	8.6	8.2	10.0	8.9
$a(^1\text{H})$	3.3	4.0	3.8	4.3	5.3	4.2	<3.5	<8.0
$a(^{99,101}\text{Ru})^b$	8.0	3.5	8.6	5.8	5.7	5.6	39 ^c	41.7 ^c

^aFrom oxidation of precursors with $\text{Fc}(\text{PF}_6)$ in CH_2Cl_2 at 298 K; coupling constants in G ($1 \text{ G} = 0.1 \text{ mT}$ or 10^{-4} T). ^b⁹⁹Ru, 12.7% natural abundance, $I = 5/2$; ¹⁰¹Ru, 17.0% natural abundance, $I = 5/2$; gyromagnetic ratio 1.12. ^c¹⁸⁹Os hyperfine coupling (¹⁸⁹Os, 16.1% natural abundance, $I = 3/2$).

ligand hyperfine structure served to assess the electronic structure of the potentially active radical intermediates.

EXPERIMENTAL SECTION

Instrumentation. X-band EPR spectra were recorded with a Bruker System EMX instrument. ¹H NMR spectra were taken on a Bruker AC 250 spectrometer. IR spectra were obtained using a Nicolet 6700 FT-IR

instrument; solid-state IR measurements were performed with an ATR unit (smart orbit with diamond crystal). UV–vis–NIR absorption spectra were recorded on J&M TIDAS and Shimadzu UV 3101 PC spectrophotometers. Cyclic voltammetry was carried out in 0.1 M Bu_4NPF_6 solutions using a three-electrode configuration (glassy-carbon working electrode, Pt counter electrode, Ag/AgCl reference electrode) and a PAR 273 potentiostat and function generator. The ferrocene/ferrocenium (Fc/Fc^+) couple served as internal reference. Simulation

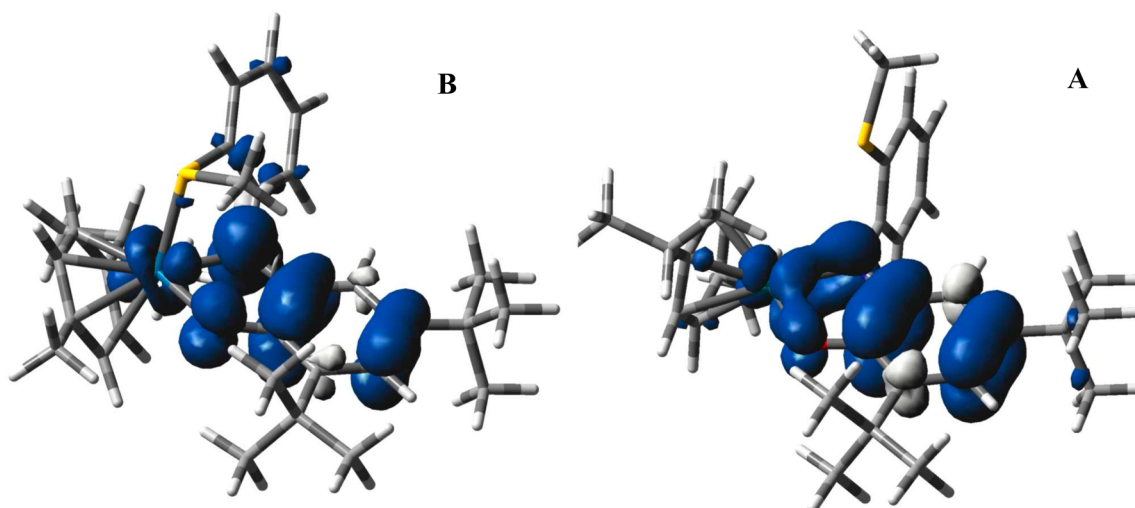


Figure 11. DFT (G09/PBE0/PCM) calculated spin densities for forms B (left) and A (right) of 1^+ .

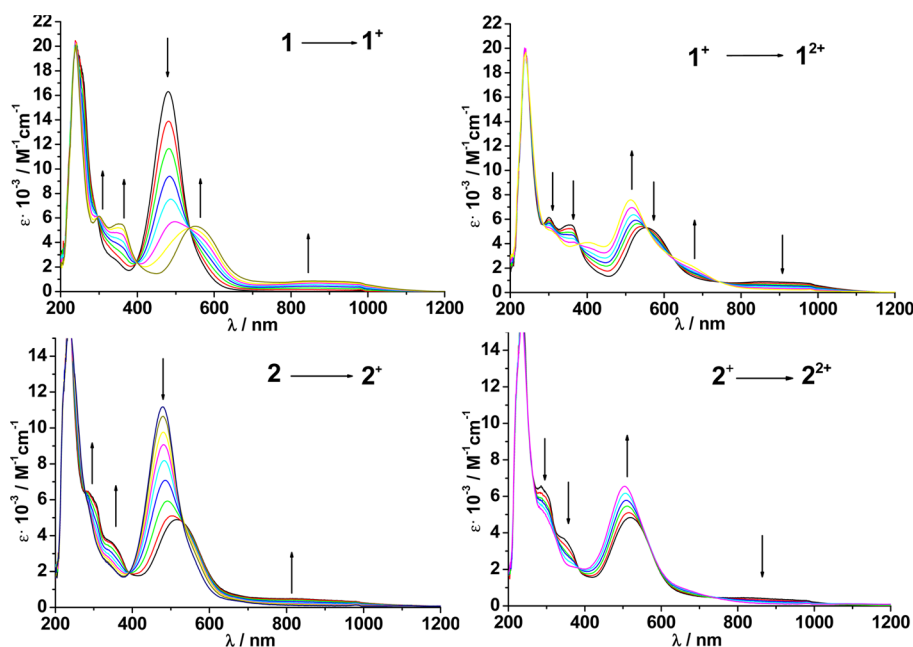


Figure 12. UV-vis-NIR spectroelectrochemical responses of compounds 1 and 2 to their stepwise one- and two-electron oxidations in $\text{CH}_2\text{Cl}_2/0.1 \text{ M Bu}_4\text{NPF}_6$ at 298 K.

curves were acquired using the DigiElch 7.0 version²⁵ to investigate the redox mechanism and to establish the kinetic parameters for electrochemical and chemical steps. Diffusion coefficients were determined by Cottrell type plots (Figure S16 (Supporting Information)). Spectroelectrochemistry was performed using an optically transparent thin-layer electrode (OTTLE) cell at room temperature and a cryostated cell at low temperatures.⁹ Thin-layer cyclic voltammograms were recorded in the course of the spectroelectrochemical monitoring. A two-electrode capillary served to generate intermediates for X-band EPR studies.²⁶

Synthesis. All reactions were conducted using Schlenk equipment. Reagents and solvents were obtained commercially and were purified by standard methods. $\text{Ru}_2\text{Cym}_2\text{Cl}_4$ was obtained from ABCR; $\text{Os}_2\text{Cym}_2\text{Br}_4$ was prepared according to ref 27.

2-Methylselenoaniline. To a solution of dimethyl diselenide (5 mmol, 0.47 mL) in 25 mL of ethanol was added NaBH_4 (10.9 mmol, 0.41 g). The solution was stirred until the color disappeared, and then 0.97 mL (9.2 mmol) of 2-fluoronitrobenzene was added. The solution was stirred for 12 h at room temperature, after which the solvent was

removed, water (20 mL) was added, and the product was extracted with dichloromethane. The organic phase was dried over MgSO_4 , and the crude product was reacted for the next step without further purification. A suspension of methylseleno-2-nitrobenzene (8 mmol), zinc powder (75 mmol, 4.9 g), and ammonium chloride (48 mmol, 2.6 g) in THF (70 mL) were stirred for 20 h at reflux under an argon atmosphere. The resulting suspension was filtered and the solid washed with dichloromethane. The organic phase was dried over MgSO_4 , the solvent was removed, and the product was purified over a silica column (hexane/ethyl acetate 1/1). Yield: 53% (4.24 mmol) of an orange oil. Anal. Calcd for $\text{C}_7\text{H}_9\text{NSe}$: C, 45.17; H, 4.87; N, 7.53. Found: C, 45.66; H, 4.96; N, 7.70. $^1\text{H NMR}$ (250 MHz, CD_2Cl_2): δ 7.49 (dd, $J = 7.7, 1.6$ Hz, 1H), 7.13 (ddd, $J = 8.0, 7.3, 1.6$ Hz, 1H), 6.77 (dd, $J = 8.0, 1.3$ Hz, 1H), 6.67 (td, $J = 7.5, 1.4$ Hz, 1H), 4.34 (s, 2H), 2.25 (t, 3H, $J = 5.7$ Hz zu ^{77}Se). $^{13}\text{C NMR}$ (63 MHz, CD_2Cl_2): δ 147.9, 135.8, 129.3, 118.5, 115.3, 114.3, 7.8. $^{77}\text{Se NMR}$ (47.7 MHz, CD_2Cl_2): δ 100.54.

Q_{SeMe} Procedure as described for Q_{SMe} ,⁷ using 2-methylselenoaniline. Anal. Calcd for $\text{C}_{13}\text{H}_{29}\text{NOSe}$: C, 64.60; H, 7.49; N, 3.59. Found: C, 64.55; H, 7.50; N, 3.52. $^1\text{H NMR}$ (250 MHz, C_6D_6): δ 7.54 (dd, $J = 7.6,$

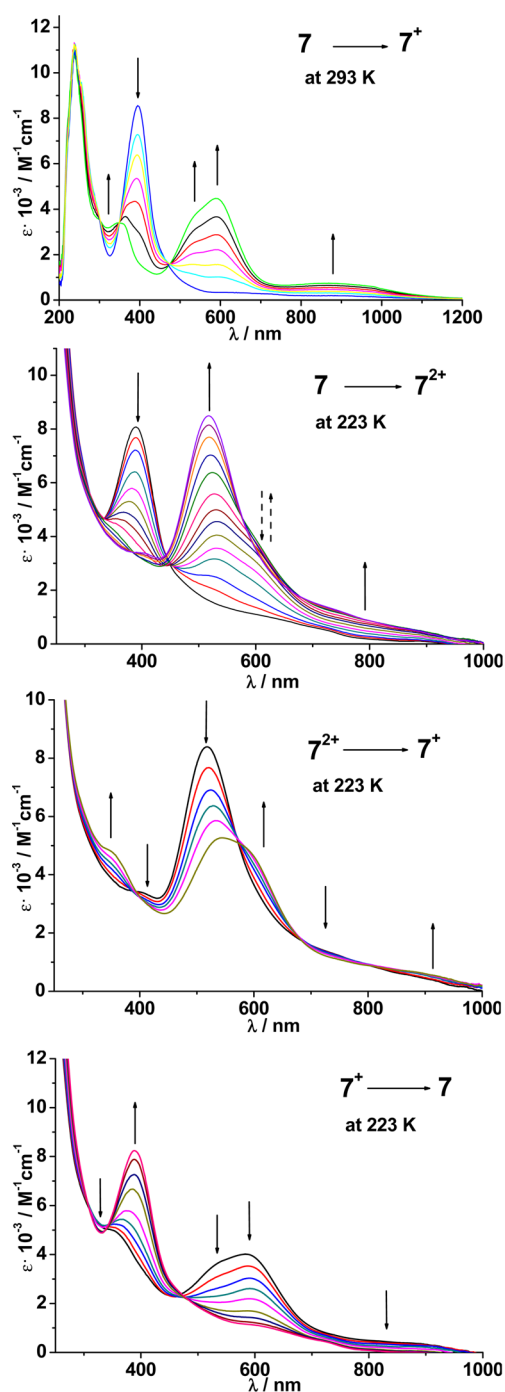


Figure 13. UV-vis-NIR spectroelectrochemical responses of **7** to its one- and two-electron oxidations and reverse reductions in $\text{CH}_2\text{Cl}_2/0.1 \text{ M Bu}_4\text{NPF}_6$ at 298 K (top) and 223 K (bottom). See the main text for an explanation.

1.4 Hz, 1H), 7.47 (d, $J = 2.3$ Hz, 1H), 7.02 (d, $J = 2.7$ Hz, 1H), 6.94–6.80 (m, 1H), 6.65–6.50 (m, 2H), 6.33 (s, 1H), 6.02 (s, 1H), 1.75 (s, 3H), 1.65 (s, 9H), 1.23 (s, 9H). ^{13}C NMR (63 MHz, C_6D_6): δ 150.0, 148.0, 142.3, 136.1, 135.4, 129.9, 122.1, 122.0, 120.1, 117.5, 113.9, 35.0, 34.1, 31.4, 29.5, 7.8. ^{77}Se (47.7 MHz, CD_2Cl_2): δ 94.9.

General Procedure for the Synthesis of 1–9. $\text{M}_2\text{Cym}_2\text{X}_4$ (0.08 mmol) and H_2Q (0.16 mmol)⁷ were dissolved in 10 mL of dichloromethane/*n*-hexane (1/1). To this solution was added 0.5 mL (3.5 mmol) of Et_3N . The orange solution turned dark red immediately. The reaction mixture was stirred for 1 h, and then the solvent was evaporated under reduced pressure. The red residue was extracted into 100 mL of *n*-hexane and the solid Et_3NHCl removed by filtration. The

solvent was removed to obtain a dark red, air-sensitive residue. Yields: **1**, 68% (63 mg); **2**, 77% (69 mg); **3**, 70% (70 mg); **4**, 82% (69 mg); **5**, 86% (78 mg); **6**, 69% (64 mg); **7**, 51% (54 mg); **8**, 59% (61 mg); **9**, 48% (55 mg).

Compound 1. Anal. Calcd (found) for **1**, $\text{C}_{31}\text{H}_{41}\text{NORuS}$ (576.78): C, 64.22; H, 7.16; N, 2.43. Found: C, 65.20; H, 7.55; N, 2.59. ^1H NMR (250 MHz, C_6D_6): δ 7.37 (d, $J^3 = 2.2$ Hz, 1H, Ar-H), 7.10 (m, 3H, Ar-H), 6.84 (d, $J^3 = 2.1$ Hz, 1H, Ar-H), 5.18 (d, $J^3 = 5.5$ Hz, 1H, Cym-H), 5.04 (d, $J^3 = 5.5$ Hz, 1H, Cym-H), 4.74 (d, $J^3 = 5.7$ Hz, 1H, Cym-H), 4.70 (d, $J^3 = 5.8$ Hz, 1H, Cym-H), 2.58 (sep, $J = 2.2$ Hz, 1H, $\text{CH}(\text{CH}_3)_2$), 1.88 (s, 9H, $\text{C}(\text{CH}_3)_3$), 1.87 (s, 3H, SCH_3), 1.56 (s, 3H, CH_3), 1.32 (s, 9H, $\text{C}(\text{CH}_3)_3$), 1.25 (d, $J = 3.1$ Hz, 3H, $\text{CH}(\text{CH}_3)_2$), 1.23 (d, $J = 3.2$ Hz, 3H, $\text{CH}(\text{CH}_3)_2$). ESI-MS: m/z calcd for $\text{C}_{31}\text{H}_{41}\text{NORuS} + \text{H}^+$ (found) 577.195 (577.195).

Compound 2. Anal. Calcd (found) for **2**, $\text{C}_{31}\text{H}_{41}\text{NO}_2\text{Ru}$ (560.72): C, 66.40; H, 7.37; N, 2.50. Found: C, 66.70; H, 7.50; N, 2.49. ^1H NMR (250 MHz, C_6D_6): δ 7.35 (d, $J = 2.2$ Hz, 1H, Ar-H), 7.28 (dd, $J = 7.6, 1.7$ Hz, 1H, Ar-H), 7.10 (dd, $J = 8.0, 1.7$ Hz, 1H, Ar-H), 6.95 (dd, $J = 7.5, 1.3$ Hz, 1H, Ar-H), 6.91 (d, $J = 2.2$ Hz, 1H, Ar-H), 6.75 (dd, $J = 8.1, 1.1$ Hz, 1H, Ar-H), 5.05 (d, $J = 5.6$ Hz, 1H, Cym-H), 4.98 (d, $J = 5.7$ Hz, 1H, Cym-H), 4.76 (d, $J = 5.7$ Hz, 1H, Cym-H), 4.64 (d, $J = 5.7$ Hz, 1H, Cym-H), 3.18 (s, 3H, OCH_3), 2.44 (sep, $J = 6.6$ Hz, 1H, $\text{CH}(\text{CH}_3)_2$), 1.86 (s, 9H, $\text{C}(\text{CH}_3)_3$), 1.62 (s, 3H, CH_3), 1.33 (s, 9H, $\text{C}(\text{CH}_3)_3$), 1.19 (dd, $J = 6.6$ Hz, 6H, $\text{CH}(\text{CH}_3)_2$). ESI-MS: m/z calcd for $\text{C}_{31}\text{H}_{41}\text{NO}_2\text{Ru} + \text{H}^+$ (found) 561.220 (561.219).

Compound 3. Anal. Calcd (found) for **3**, $\text{C}_{31}\text{H}_{41}\text{NORuSe}$ (625.69): C, 59.70; H, 6.63; N, 2.25. Found: C, 60.01; H, 6.77; N, 2.20. ^1H NMR (400 MHz, C_6D_6): δ 7.35 (d, $J = 2.2$ Hz, 2H, Ar-H), 7.11–7.00 (m, 4H, Ar-H), 6.84 (d, $J = 2.2$ Hz, 2H, Ar-H), 5.21 (d, $J = 5.6$ Hz, 1H, Cym-H), 5.03 (d, $J = 5.4$ Hz, 1H, Cym-H), 4.75 (d, $J = 5.8$ Hz, 1H, Cym-H), 4.70 (d, $J = 5.6$ Hz, 1H, Cym-H), 2.60 (sept, 6.6 Hz, 1H, $\text{CH}(\text{CH}_3)_2$), 1.86 (s, 9H, $\text{C}(\text{CH}_3)_3$), 1.73 (s, 3H, SeCH_3), 1.54 (s, 3H, Ar- CH_3), 1.30 (s, 9H, $\text{C}(\text{CH}_3)_3$), 1.24 (d, 6.6 Hz, 6H, $\text{CH}(\text{CH}_3)_2$), 1.21 (d, 6.6 Hz, 6H, $\text{CH}(\text{CH}_3)_2$). ESI-MS: m/z calcd for $\text{C}_{31}\text{H}_{41}\text{NORuSe}^+$ (found) 625.1 (625.2).

Compound 4. Anal. Calcd (found) for **4**, $\text{C}_{30}\text{H}_{39}\text{NORu}$ (530.70): C, 69.08; H, 8.08; N, 2.44. Found: C, 68.97; H, 8.07; N, 2.33. ^1H NMR (250 MHz, C_6D_6): δ 7.37 (d, $J = 2.2$ Hz, 1H, Ar-H), 7.29–7.16 (m, 2H, Ar-H), 7.07 (dt, $J = 4.7, 2.0$ Hz, 1H, Ar-H), 7.03 (d, $J = 2.1$ Hz, 1H, Ar-H), 4.97 (d, $J = 6.0$ Hz, 1H, Cym-H), 4.62 (d, $J = 6.0$ Hz, 1H, Cym-H), 2.38 (sep, $J = 6.9$ Hz, 1H, $\text{CH}(\text{CH}_3)_2$), 1.88 (s, 9H, $\text{C}(\text{CH}_3)_3$), 1.50 (s, 3H, CH_3), 1.30 (s, 9H, $\text{C}(\text{CH}_3)_3$), 1.14 (d, $J = 6.9$ Hz, 6H, $\text{CH}(\text{CH}_3)_2$). ESI-MS: m/z calcd for $\text{C}_{30}\text{H}_{39}\text{NORu}^+$ (found) 531.208 (531.208).

Compound 5. Anal. Calcd (found) for **5**, $\text{C}_{31}\text{H}_{38}\text{F}_3\text{NORu}$ (598.69): C, 63.63; H, 7.07; N, 2.18. Found: C, 63.17; H, 7.15; N, 2.17. ^1H NMR (250 MHz, C_6D_6): δ 7.60 (m, 1H, Ar-H), 7.37 (d, $J = 2.1$ Hz, 1H, Ar-H), 7.27 (d, $J = 7.8$ Hz, 1H, Ar-H), 7.23 (d, $J = 8.6$ Hz, 1H, Ar-H), 6.99 (t, $J = 7.8$ Hz, 1H, Ar-H), 6.90 (d, $J = 2.1$ Hz, 1H, Ar-H), 4.91 (m, 2H, Cym-H), 4.59 (d, $J = 5.7$ Hz, 1H, Cym-H), 4.54 (d, $J = 5.7$ Hz, 1H, Cym-H), 2.31 (sept, $J = 6.9$ Hz, 1H, $\text{CH}(\text{CH}_3)_2$), 1.88 (s, 9H, $\text{C}(\text{CH}_3)_3$), 1.41 (s, 3H, CH_3), 1.28 (s, 9H, $\text{C}(\text{CH}_3)_3$), 1.09 (d, $J = 6.9$ Hz, 6H, $\text{CH}(\text{CH}_3)_2$). ESI-MS: m/z calcd for $\text{C}_{31}\text{H}_{38}\text{F}_3\text{NORu}^+$ (found) 599.19 (599.19).

Compound 6. Anal. Calcd (found) for **6**, $\text{C}_{32}\text{H}_{43}\text{NORu}$ (558.75): C, 68.78; H, 7.76; N, 2.51. Found: C, 68.53; H, 7.85; N, 2.38. ^1H NMR (250 MHz, CD_2Cl_2): δ 7.41 (dd, $J = 5.1, 4.1$ Hz, 1H, Ar-H), 7.35–7.20 (m, 3H, Ar-H), 6.92 (d, $J = 2.2$ Hz, 1H, Ar-H), 6.34 (d, $J = 2.1$ Hz, 1H, Ar-H), 5.42 (d, $J = 5.7$ Hz, 1H, Cym-H), 5.07 (d, $J = 5.7$ Hz, 1H, Cym-H), 5.00 (d, $J = 5.7$ Hz, 1H, Cym-H), 2.80–2.65 (sep, 1H, $\text{CH}(\text{CH}_3)_2$), 2.52–2.33 (quint, 2H, Ar- CH_2CH_3), 1.54 (s, 9H, $\text{C}(\text{CH}_3)_3$), 1.43–1.31 (m, 6H, $\text{CH}(\text{CH}_3)_2$), 1.16–1.06 (m, 11H, Ar- CH_2CH_3 and $\text{C}(\text{CH}_3)_3$). ESI-MS: m/z calcd for $\text{C}_{32}\text{H}_{43}\text{NORu}^+$ (found) 559.24 (559.24).

Compound 7. Anal. Calcd (found) for **7**, $\text{C}_{31}\text{H}_{41}\text{NOOS}$ (665.96): C, 55.91; N, 6.21; H, 2.10. Found: C, 55.45; N, 6.21; H, 2.20. ^1H NMR (250 MHz, C_6D_6): δ 7.23 (d, $J = 2.2$ Hz, 1H, Ar-H), 7.06–6.99 (m, 4H, Ar-H), 6.86 (d, $J = 2.1$ Hz, 1H, Ar-H), 5.67 (d, $J = 5.4$ Hz, 1H, Cym-H), 5.46 (d, $J = 5.4$ Hz, 1H, Cym-H), 5.25 (d, $J = 5.4$ Hz, 1H, Cym-H), 5.16 (d, $J = 5.4$ Hz, 1H, Cym-H), 2.49 (sep, $J = 6.9$ Hz, 1H, $\text{CH}(\text{CH}_3)_2$), 1.87–1.82 (m, $J = 4.1$ Hz, 12H, SCH_3 , $\text{C}(\text{CH}_3)_3$), 1.66 (s, 3H, Cym- CH_3), 1.33 (s, 9H, $\text{C}(\text{CH}_3)_3$), 1.24 (d, $J = 3.2$ Hz, 3H, $\text{CH}(\text{CH}_3)_2$), 1.21

Table 5. UV–Vis Absorption Maxima $\lambda_{\text{max}}/\text{nm}$ ($\epsilon/\text{M}^{-1} \text{cm}^{-1}$) from Spectroelectrochemistry in $\text{CH}_2\text{Cl}_2/0.1 \text{ M Bu}_4\text{NPF}_6$

compound	$\lambda_{\text{max}}/\text{nm}$ ($\epsilon/\text{M}^{-1} \text{cm}^{-1}$)
1	344 (1870), 480 (11870)
1 ⁺	298 (4470), 355 (4010), 552 (3860), 700–1000 (<670)
1 ²⁺	309 (3830), 404 (3040), 513 (5580), 674 (1680)
2	343 (11000), 481 (1650)
2 ⁺	284 (7850), 343 (3580), 500 (4380), 540 (4090), 654 (2400), 700–1000 (<590)
2 ²⁺	294 (5080), 505 (5630)
3	343 (2350), 481 (12500)
3 ⁺	296 (4960), 354 (4730), 542 (4490), 593 (3390), 700–1000 (<960)
3 ²⁺	392 (3630), 517 (7760), 709 (1150)
4	347 (1980), 478 (13610)
4 ⁺	301 (4700), 367 (3550), 486 (6520), 700–1000 (<670)
4 ²⁺	305 (3750), 480 (6270), 636 (1590)
5	348 (2430), 480 (13810)
5 ⁺	293 (5510), 358 (3860), 488 (7160), 700–1000 (<520)
5 ²⁺	304 (4140), 481 (7590), 641 (1110)
6	339 (2180), 478 (11000)
6 ⁺	306 (2290), 356 (3840), 488 (5120), 700–1000 (<660)
6 ²⁺	379 (1920), 540 (5278)
7	395 (8240)
7 ⁺	351 (4980), 535 (3650), 582 (4010), 700–1000 (<550)
7 ²⁺	397 (3760), 517 (8390)
8	391 (8260)
8 ⁺	354 (3290), 518 (7580), 700–100 (<780)
8 ²⁺	364 (3860), 513 (5380)
9	395 (7810)
9 ⁺	361 (3870), 526 (3600), 581 (4500), 700–1000 (<700)
9 ²⁺	398 (2940), 515 (8540)

($d, J = 3.2 \text{ Hz}$, 3H, $\text{CH}(\text{CH}_3)_2$). ESI-MS: m/z calcd for $\text{C}_{31}\text{H}_{41}\text{NOOs}^+$ (found) 667.25 (667.25).

Compound 8. Anal. Calcd (found) for **8**, $\text{C}_{31}\text{H}_{41}\text{NO}_2\text{Os}$ (649.89): C, 57.29; N, 6.36; H, 2.16. Found: C, 59.68; N, 7.45; H, 2.06. $^1\text{H NMR}$ (250 MHz, C_6D_6): δ 7.23–7.16 (m, $J = 8.1, 2.0 \text{ Hz}$, 1H, Ar-H), 7.07–6.99 (m, 1H, Ar-H), 6.93–6.84 (m, 1H, Ar-H), 6.73–6.66 (m, 1H, Ar-H), 5.52 (d, $J = 5.4 \text{ Hz}$, 1H, Cym-H), 5.40 (d, $J = 5.4 \text{ Hz}$, 1H, Cym-H), 5.23 (d, $J = 5.4 \text{ Hz}$, 1H, Cym-H), 5.07 (d, $J = 5.4 \text{ Hz}$, 1H, Cym-H), 3.15 (s, 3H, OCH_3), 2.31 (sep, $J = 6.9$, 1H, $\text{CH}(\text{CH}_3)_2$), 1.81 (s, 9H, $\text{C}(\text{CH}_3)_3$), 1.73 (s, 3H, CH_3), 1.35 (s, 9H, $\text{C}(\text{CH}_3)_3$), 1.20–1.14 (m, 6H, $\text{CH}(\text{CH}_3)_2$). ESI-MS: m/z calcd for $\text{C}_{31}\text{H}_{41}\text{NO}_2\text{Os}^+$ (found) 651.27 (651.27).

Compound 9. Anal. Calcd (found) for **9**, $\text{C}_{31}\text{H}_{41}\text{NOOsSe}$ (712.85): C, 52.23; N, 5.81; H, 1.96. Found: C, 51.79; N, 5.74; H, 1.90. $^1\text{H NMR}$ (250 MHz, C_6D_6): δ 7.27 (d, $J = 2.2 \text{ Hz}$, 1H, Ar-H), 7.03 (m, 4H, Ar-H), 6.93 (d, $J = 2.2 \text{ Hz}$, 1H, Ar-H), 5.76 (d, $J = 5.4 \text{ Hz}$, 1H, Cym-H), 5.48 (d, $J = 5.4 \text{ Hz}$, 1H, Cym-H), 5.31 (d, $J = 5.5 \text{ Hz}$, 1H, Cym-H), 5.18 (d, $J = 5.4 \text{ Hz}$, 1H, Cym-H), 2.53 (sept, $J = 13.7, 6.8 \text{ Hz}$, 1H, $\text{CH}(\text{CH}_3)_2$), 1.87 (s, 9H, $\text{C}(\text{CH}_3)_3$), 1.66 (d, $J = 3.5 \text{ Hz}$, 6H, SeCH_3), 1.38 (d, $J = 3.2 \text{ Hz}$, 9H, $\text{C}(\text{CH}_3)_3$), 1.31–1.23 (m, 6H, $\text{CH}(\text{CH}_3)_2$). ESI-MS: m/z calcd for $\text{C}_{31}\text{H}_{41}\text{NOOsSe}^+$ (found) 715.19 (715.19).

[1](BAR^F). A 75 mg amount (0.13 mmol) of **1** was dissolved in CH_2Cl_2 (8 mL). To this solution was added $\text{Fc}(\text{BAR}^{\text{F}})$ (0.13 mmol, 133 mg).^{12c} The red solution turned purple immediately and was subsequently stirred for 1 h at room temperature. The solvent was removed, and the purple solid was washed three times with 6 mL of *n*-hexane. The complex was dissolved in diethyl ether, precipitated with hexane, and filtered. The complex was crystallized from benzene at 8 °C. Anal. Calcd for $\text{C}_{63}\text{H}_{53}\text{BF}_{24}\text{NORuS}$ (1440.00): C, 52.55; N, 0.97; H, 3.71; S, 2.23. Found: C, 52.42; N, 1.04; H, 3.69; S, 2.36. ESI-MS: m/z calcd for $\text{C}_{31}\text{H}_{41}\text{NORuS}^+$ (found): 577.20 (577.20) and $\text{C}_{32}\text{H}_{42}\text{BF}_{24}^-$ (found): 863.06 (863.07).

[3](BAR^F). The procedure was analogous to that for **[1](BAR^F)**, using **3**. Anal. Calcd for $\text{C}_{63}\text{H}_{53}\text{BF}_{24}\text{NORuSe}$ (1486.90): C, 50.89; N, 0.94; H, 3.59. Found: C, 51.18; N, 0.89; H, 3.70. ESI-MS: m/z calcd for $\text{C}_{31}\text{H}_{41}\text{NORuSe}^+$ (found): 625.1 (625.1).

Crystallography. Crystals suitable for X-ray diffraction were prepared by slow crystallization from pentane or diethyl ether solutions at $-34 \text{ }^\circ\text{C}$ in the case of the neutral metal compounds and from benzene at $8 \text{ }^\circ\text{C}$ for the cationic forms. Crystals of **[10](PF₆)** suitable for X-ray diffraction were obtained from a dichloromethane solution at $8 \text{ }^\circ\text{C}$. X-ray diffraction data were collected using a Bruker Kappa Apex2duo diffractometer. The structures were solved and refined by full-matrix least-squares techniques on F^2 using the SHELX-97 program.²⁸ The absorption corrections were done by the multiscan technique or by numeric means (see the Supporting Information). All non-hydrogen atoms were refined anisotropically, except for the partially occupied split F atom positions in the BAR^{F} anions. Hydrogen atoms were included in the refinement process as per the riding model. The structures of **[1](BAR^F)**, **[3](BAR^F)**, and **[10](PF₆)** contain large voids which contain highly disordered solvent molecules (benzene in the case of **[1](BAR^F)** and **[3](BAR^F)** or dichloromethane in the case of **[10](PF₆)**). Since the solvent molecules could not be located, the PLATON/SQUEEZE procedure²⁹ was used. In the structure of **6** one of the two independent molecules has an isopropyl group, which was modeled with 50% occupied split positions (C139 and C140).

DFT Calculations. The electronic structures of the complexes $[\text{Ru}(\text{Cym})\text{Q}]^n$ and $[\text{Os}(\text{Cym})\text{Q}]^n$ in the neutral and the monooxidized states were calculated by density functional theory (DFT) methods using the Gaussian 09³⁰ (G09) program package.

Within the G09 calculations, quasi-relativistic effective core pseudopotentials and the corresponding optimized set of basis functions for Ru and Os³¹ and 6-311G(d) polarized triple- ζ basis sets³² for the remaining atoms were employed. G09 calculations employed the hybrid exchange and correlation functional by Perdew, Burke, and Ernzerhof.^{33,34} The solvent was described by the polarizable calculation model (PCM).³⁵ The geometry optimizations were performed both in vacuo and with PCM correction. Geometry optimizations were followed by vibrational analysis; no imaginary frequencies were found for the optimized structures. Electronic excitations were calculated by the time-dependent DFT (TD DFT) method.

■ ASSOCIATED CONTENT

■ Supporting Information

CIF files giving crystallographic data for $[\text{Ru}(\text{Cym})(\text{Q}_{\text{SMe}})]$, $[\text{Ru}(\text{Cym})(\text{Q}_{\text{SMe}})]^+$, $[\text{Ru}(\text{Cym})(\text{Q}_{\text{OMe}})]$, $[\text{Ru}(\text{Cym})(\text{Q}_{\text{SeMe}})]$, $[\text{Ru}(\text{Cym})(\text{Q}_{\text{SeMe}})]^+$, $[\text{Ru}(\text{Cym})(\text{Q}_{\text{H}})]$, $[\text{Ru}(\text{Cym})(\text{Q}_{\text{3-CF}_3})]$, and $[\text{Ru}(\text{Cym})(\text{Q}_{\text{Et}})]$, crystallographic data (Table S1), selected atom–atom distances (Å) and dihedral angles (deg) in $[\text{Ru}(\text{Cym})\text{Q}]^n$ complexes, comparison of experimental and DFT calculated results (Table S2), selected bond lengths (Å) and dihedral angles (deg) in complex **5**, comparison of experimental and DFT calculated results (Table S3), DFT calculated selected atom–atom distances (Å) and dihedral angles (deg) in osmium complexes (Table S4), crystallographic and refinement data of $[\text{Ru}(\text{Q}_{\text{SMe}})_2](\text{PF}_6)$ (Table S5), bond parameters for **10**⁺ and **10** (Table S6), DFT (G09/PBE0/PCM) calculated spin densities in oxidized Ru and Os complexes (Table S7), molecular structure of **3** in the crystal (Figure S1), molecular structure of **5** in the crystal (Figure S2), molecular structure of **6** in the crystal (one of two independent molecules) (Figure S3), structure of $[\text{1}](\text{BAR}^{\text{F}})$ in the crystal (Figure S4), different orientations of the *p*-cymene ligand in the crystals of **4**, **2**, and **1** (Figure S5), molecular structure of $[\text{Ru}(\text{Q}_{\text{SMe}})_2](\text{PF}_6)$ ($[\text{10}](\text{PF}_6)$) in the crystal (Figure S6), cyclic voltammograms of **2** in 0.1 M $\text{Bu}_4\text{NPF}_6/\text{CH}_2\text{Cl}_2$ at different scan rates (253 K) (Figure S7), cyclic voltammograms of **5** in 0.1 M $\text{Bu}_4\text{NPF}_6/\text{CH}_2\text{Cl}_2$ (top) and 0.1 M $\text{Bu}_4\text{NPF}_6/\text{CH}_3\text{CN}$ (bottom) (Figure S8), cyclic voltammograms of **6** in 0.1 M $\text{Bu}_4\text{NPF}_6/\text{CH}_2\text{Cl}_2$ (top) and 0.1 M $\text{Bu}_4\text{NPF}_6/\text{CH}_3\text{CN}$ (bottom) (Figure S9), differential pulse voltammogram of **1** in 0.1 M $\text{Bu}_4\text{NPF}_6/\text{CH}_2\text{Cl}_2$, scan rate 100 mV/s (Figure S10), UV–vis spectroelectrochemical response of **4** in 0.1 M $\text{Bu}_4\text{NPF}_6/\text{CH}_2\text{Cl}_2$ at 298 K (Figure S11), UV–vis–NIR spectroelectrochemical response of **5** in 0.1 M $\text{Bu}_4\text{NPF}_6/\text{CH}_2\text{Cl}_2$ at 298 K (Figure S12), UV–vis spectroelectrochemical response of **7** in 0.1 M $\text{Bu}_4\text{NPF}_6/\text{CH}_2\text{Cl}_2$ at 223 K (Figure S13), cyclic voltammograms (left) of **1** at different scan rates in 0.1 M $\text{Bu}_4\text{NPF}_6/\text{CH}_2\text{Cl}_2$ and the Cottrell plot (right) (Figure S14), and an xyz file for the calculated structures in the paper. This material is available free of charge via the Internet at <http://pubs.acs.org>.

■ AUTHOR INFORMATION

Corresponding Authors

*E-mail for F.H.: f.hartl@reading.ac.uk.

*E-mail for W.K.: kaim@iac.uni-stuttgart.de.

Notes

The authors declare no competing financial interest.

■ ACKNOWLEDGMENTS

Support from the Land Baden-Württemberg and the EU COST action programme CM1202 is gratefully acknowledged. S.Z. thanks the Ministry of Education of the Czech Republic (grant LD14129) for support. Q.Z. and F.H. acknowledge EPSRC funding (grant EP/K00753x/1) for the development of the Spectroelectrochemistry Laboratory in Reading. We also thank Dr. Wolfgang Frey (Stuttgart) for crystallographic measurements.

■ REFERENCES

(1) (a) Ringenberg, M. R.; Kokatam, S. L.; Heiden, Z. M.; Rauchfuss, T. B. *J. Am. Chem. Soc.* **2008**, *130*, 788.

(2) (a) Kaim, W. *Inorg. Chem.* **2011**, *50*, 9752. (b) Praneeth, V. K. K.; Ringenberg, M. R.; Ward, T. R. *Angew. Chem.* **2012**, *124*, 10374; *Angew. Chem., Int. Ed.* **2012**, *51*, 10228.

(3) Poddel'sky, A. I.; Cherkasov, V. K.; Abakumov, G. A. *Coord. Chem. Rev.* **2009**, *253*, 291.

(4) (a) Ringenberg, M. R.; Nilges, M. J.; Rauchfuss, T. B.; Wilson, S. R. *Organometallics* **2010**, *29*, 1956. (b) Ringenberg, M. R.; Rauchfuss, T. B. *Eur. J. Inorg. Chem.* **2012**, 490.

(5) Hübner, R.; Weber, S.; Strobel, S.; Sarkar, B.; Zálíš, S.; Kaim, W. *Organometallics* **2011**, *30*, 1414.

(6) Jeffrey, J. C.; Rauchfuss, T. B. *Inorg. Chem.* **1979**, *18*, 2658. (b) Braunstein, P.; Naud, F. *Angew. Chem.* **2001**, *113*, 702; *Angew. Chem., Int. Ed.* **2001**, *40*, 680.

(7) Ye, S.; Sarkar, B.; Lissner, F.; Schleid, Th.; van Slageren, J.; Fiedler, J.; Kaim, W. *Angew. Chem.* **2005**, *117*, 2140; *Angew. Chem., Int. Ed.* **2005**, *44*, 2103.

(8) Kaim, W.; Bubrin, M.; Hübner, R. In *Organometallic Chemistry: Recent Advances*; Pombeiro, A. J. L., Ed.; Wiley: Hoboken, NJ, 2014; p 667.

(9) (a) Krejčík, M.; Danek, M.; Hartl, F. J. *Electroanal. Chem. Interfacial Electrochem.* **1991**, *317*, 179. (b) Mahabiersing, T.; Luyten, H.; Nieuwendam, R. C.; Hartl, F. *Collect. Czech. Chem. Commun.* **2003**, *68*, 1687.

(10) (a) Thoumazet, C.; Melaimi, M.; Ricard, L.; Mathey, F.; Le Floch, P. *Organometallics* **2003**, *22*, 1580. (b) Jagadeesh, R. V.; Wienhöfer, G.; Westerhaus, F. A.; Surkus, A.-E.; Junge, H.; Hunge, K.; Beller, M. *Chem.—Eur. J.* **2011**, *17*, 14375.

(11) (a) Moitis, R. E.; Aird, R. E.; del Socorro Murdock, P.; Chen, H.; Cummings, J.; Hughes, N. D.; Parsons, S.; Parkin, A.; Boyd, G.; Jodrell, D. I.; Sadler, P. J. *J. Med. Chem.* **2001**, *44*, 3616. (b) Kandioller, W.; Hartinger, C. G.; Nazarov, A. A.; Bartel, C.; Skocic, M.; Jakupec, M. A.; Arion, V. B.; Keppler, B. K. *Chem. Eur. J.* **2009**, *15*, 12283. (c) Dorcier, A.; Dyson, P. J.; Gossens, C.; Rothlisberger, U.; Scopelliti, R.; Tavernelli, I. *Organometallics* **2005**, *24*, 2114. (d) Dralle Mjos, K.; Orvig, C. *Chem. Rev.* **2014**, *114*, 4540.

(12) (a) Yakelis, N. A.; Bergman, R. G. *Organometallics* **2005**, *24*, 8579. (b) Hayashi, Y.; Rohde, J. J.; Corey, E. J. *J. Am. Chem. Soc.* **1996**, *118*, 5502. (c) Le Bras, J.; Jiao, H.; Meyer, W. E.; Hampel, F.; Gladysz, J. A. *J. Organomet. Chem.* **2000**, *616*, 54.

(13) Hübner, R.; Sarkar, B.; Zálíš, S.; Kaim, W. *Eur. J. Inorg. Chem.* **2012**, 3569.

(14) Darensbourg, D. J.; Klausmeyer, K. K.; Reibenspies, J. H. *Inorg. Chem.* **1995**, *34*, 4676.

(15) (a) Hartl, F.; Vlček, A., Jr.; deLearie, L. A.; Pierpont, C. G. *Inorg. Chem.* **1990**, *29*, 1073. (b) Hartl, F.; Stufkens, D. J.; Vlček, A., Jr. *Inorg. Chem.* **1992**, *31*, 1687.

(16) Espinet, P.; Bailey, P. M.; Maitlis, P. M. *J. Chem. Soc., Dalton Trans.* **1979**, 1542.

(17) Chaudhuri, P.; Verani, C. N.; Bill, E.; Bothe, E.; Weyhermüller, T.; Wieghardt, K. *J. Am. Chem. Soc.* **2001**, *123*, 2213.

(18) Poddel'sky, A. I.; Cherkasov, V. K.; Abakumov, G. A. *Coord. Chem. Rev.* **2009**, *253*, 291.

(19) Brown, S. N. *Inorg. Chem.* **2012**, *51*, 1251.

(20) Miller, J. S.; Min, K. S. *Angew. Chem.* **2009**, *121*, 268; *Angew. Chem., Int. Ed.* **2009**, *48*, 262.

(21) Weil, J. A.; Bolton, J. R. *Electron Paramagnetic Resonance*, 2nd ed.; Wiley: Hoboken, NJ, 2007.

(22) Kaim, W.; Sarkar, B. *Coord. Chem. Rev.* **2013**, *257*, 1650.

(23) Kaim, W. *Coord. Chem. Rev.* **1987**, *76*, 187.

(24) (a) Sembiring, S. M.; Colbran, S. B.; Craig, D. C. *Inorg. Chem.* **1995**, *34*, 761. (b) He, Z.; Colbran, S. B.; Craig, D. C. *Chem. Eur. J.* **2003**, *9*, 116. (c) Leconte, N.; Ciccione, J.; Gellon, G.; Philouze, C.; Thomas, F. *Chem. Commun.* **2014**, *50*, 1918.

(25) Nica, S.; Rudolph, M.; Görls, H.; Plass, W. *Inorg. Chim. Acta* **2007**, *360*, 1743.

(26) Kaim, W.; Ernst, S.; Kasack, V. *J. Am. Chem. Soc.* **1990**, *112*, 173.

(27) Clayton, H. S.; Makhubela, B. C. E.; Su, H.; Smith, G. S.; Moss, J. R. *Polyhedron* **2009**, *28*, 1511.

(28) Sheldrick, G. M. *SHELXL-97: Program for Crystal Structure Determination*; University of Göttingen, Göttingen, Germany, 1997.

(29) Spek, A. L. *Acta Crystallogr., Sect. D* **2009**, *65*, 148.

(30) Frisch, M. J.; Trucks, G. W.; Schlegel, H. B.; Scuseria, G. E.; Robb, M. A.; Cheeseman, J. R.; Scalmani, G.; Barone, V.; Mennucci, B.; Petersson, G. A.; Nakatsuji, H.; Caricato, M.; Li, X.; Hratchian, H. P.; Izmaylov, A. F.; Bloino, J.; Zheng, G.; Sonnenberg, J. L.; Hada, M.; Ehara, M.; Toyota, K.; Fukuda, R.; Hasegawa, J.; Ishida, M.; Nakajima, T.; Honda, Y.; Kitao, O.; Nakai, H.; Vreven, T.; Montgomery, J. A., Jr.; Peralta, J. E.; Ogliaro, F.; Bearpark, M.; Heyd, J. J.; Brothers, E.; Kudin, K. N.; Staroverov, V. N.; Kobayashi, R.; Normand, J.; Raghavachari, K.; Rendell, A.; Burant, J. C.; Iyengar, S. S.; Tomasi, J.; Cossi, M.; Rega, N.; Millam, J. M.; Klene, M.; Knox, J. E.; Cross, J. B.; Bakken, V.; Adamo, C.; Jaramillo, J.; Gomperts, R.; Stratmann, R. E.; Yazyev, O.; Austin, A. J.; Cammi, R.; Pomelli, C.; Ochterski, J. W.; Martin, R. L.; Morokuma, K.; Zakrzewski, V. G.; Voth, G. A.; Salvador, P.; Dannenberg, J. J.; Dapprich, S.; Daniels, A. D.; Farkas, O.; Foresman, J. B.; Ortiz, J. V.; Cioslowski, J.; Fox, D. J. *Gaussian 09, Revision C.01*; Gaussian, Inc., Wallingford, CT, 2009.

(31) te Velde, G.; Bickelhaupt, F. M.; van Gisbergen, S. J. A.; Fonseca Guerra, C.; Baerends, E. J.; Snijders, J. G.; Ziegler, T. *J. Comput. Chem.* **2001**, *22*, 931.

(32) Curtiss, L. A.; McGrath, M. P.; Blaudeau, J.-P.; Davis, N. E.; Binning, R. C., Jr.; Radom, L. *J. Chem. Phys.* **1995**, *103*, 6104.

(33) Perdew, J. P.; Burke, K.; Ernzerhof, M. *Phys. Rev. Lett.* **1996**, *77*, 3865.

(34) Adamo, C.; Barone, V. *J. Chem. Phys.* **1999**, *110*, 6158.

(35) Cossi, M.; Rega, N.; Scalmani, G.; Barone, V. *J. Comput. Chem.* **2003**, *24*, 669.